SCIENCE SET
OPEN ACCESS PUBLISHERS

Research Article

Journal of Subsurface Energy, Fluids, and Environmental Systems

Appraisal of Structures, Alteration And Deformational Phases of Rambi Gold Target, Western Kenya

Maryce Nandeche Obindah[1]*, Christopher Nyamai[2] & Josphat Mulwa[3]

[1]*Department of Earth and Climate Sciences, University of Nairobi, P.O Box 30197, Nairobi Kenya*
[2]*Department of Earth and Climate Sciences, University of Nairobi, P.O Box 30197, Nairobi Kenya*
[3]*Department of Earth and Climate Sciences, University of Nairobi, P.O Box 30197, Nairobi Kenya*

***Corresponding author:** Maryce Nandeche Obindah, Department of Earth and Climate Sciences, University of Nairobi, P.O Box 30197, Nairobi Kenya,

Submitted: 28 October 2025 **Accepted:** 04 November 2025 **Published:** 11 November 2025

https://doi.org/10.63620/MKJSEFES.2025.

Citation: *Obindah, M. N., Nyamaib, C., & Mulwa, J. (2025) Appraisal of Structures, Alteration And Deformational Phases of Rambi Gold Target, Western Kenya, J. Subsurf. Energy Fluids Environ. Syst, (1)1. 01-14.*

Abstract

Rambi gold prospect is located in southwest of Busia-Kakamega Greenstone Belt. The target lies at the intersection of latitude 0° 3′ 59.53″N longitude 40° 19′ 6.80″E and has been worked for gold since the 1930s. As promulgated by the colonialists, the mineralization model conforms to a quartz-vein-hosted gold system lying within a shear zone. Besides this compact historical information, Rambi as a target lacks sufficient geological information to advance mineral exploration. This study was set to appraise the gold prospectivity of Rambi as a target through an integrated modernized exploration approach. This approach was aided majorly by assessing the Airborne magnetic and geochemical datasets. Through the investigation of magnetic data, geological structural pattern encompassing mineralization was realized through enhancement of the primary images. Geochemically, X-Ray Diffraction analysis of eight representative samples in this study were successfully carried out to investigate alteration minerals. Illite and kaolinite stand out as major clay alteration minerals over the sheared/altered potential zones. Petrographic analysis of altered rock samples elucidated the alteration level of the rocks. Shear lineaments reveal two main deformation episodes in the area as supported by analysis from the fabric diagrams (Rose Diagram). Majorly, the lineaments are grouped into Deformation-1 (D1), Deformation-2 (D2) and Deformation-3 (D3) following the different deformational phases in relation to one another. Major finding are the two main internal shear structures of approximately 1Km strike length, located within the main shear. Similar comparative structures have been attributed to many of the world-class ore deposits, e.g. the Kundana Goldfield in Western, Australia.

Keywords: Gold, Structure, Alteration, Deformational Phases, Greenstone Belt, Western Kenya

Introduction

Rambi Prospect, originally a colonial mine, is located in western Kenya (Figure 1), bordering other gold prospects (e.g., Abom, Aila, Ramba-Lumba, Kakumu). Geologically, they are all located within the Tanzanian Craton, which is fused to other neighboring cratons by Proterozoic mobile belts. This geological setup represents a favorable geodynamic setting for orogenic and intrusion-related gold mineralization. Despite the favorable setting for gold deposits in western Kenya and evidence of existing old colonial and active artisanal mining activities, efforts still need to be made towards establishing potential world-class gold deposits in the region.

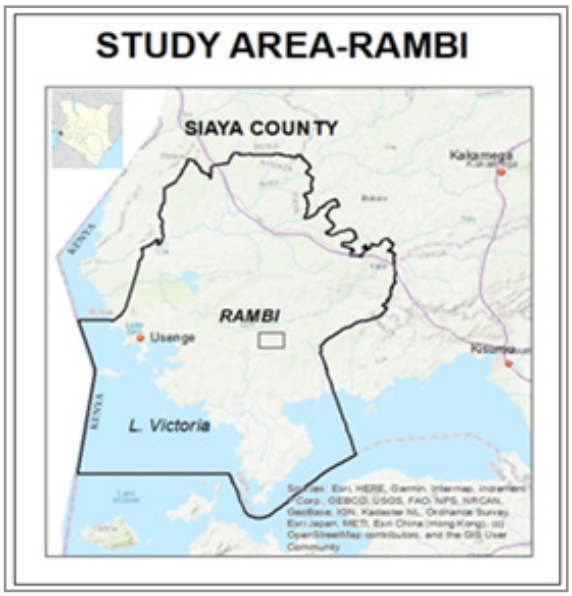

Figure 1: Location of Rambi Prospect in Siaya county, Western Kenya

Rambi colonial mine was operational from the 1930s to the 1960s, with production recorded to be 3175 Oz (98.7 Kg) of gold from 1935 to 1937(retrieved information from the level and plan maps of the colonial maps). Essential details of mine geology are not precise, but the ore is described as having "multiple quartz veins of up to 5m width develop in shear zones, what was known as the "Fabal reef" by the colonial miners. This information led to a historical data review that was completed before the commencement of the recent 2018 diamond drilling programme. The objectives fell short when all three Diamond-drilled holes did not hit the anticipated target zones.

One major characteristic of the ore from this description is that the ore is structurally aligned within sheared zones in the rocks. There is however need for studies to be done to confirm these zones of shearing and the general structural alignment of the target. Hence, the aim of the study is to appraise the understanding of gold mineralization in Rambi by assessing the structures, hydrothermal alteration and the deformational phases of the host rocks.

The specific objectives include the three outlined below.

1. Assess the existence and orientation of the inherent gold-bearing structures from the colonial miners' description
2. Examine the evident hydrothermal fluid interaction with the rocks within the Rambi target of its sufficiency to promote gold mineralization
3. Analyze the state of rock deformation at Rambi if favorable for gold mineralization.

Literature Review

Busia-Kakamega Greenstone Belt as a section of the Lake Victoria Goldfield (LVG) extends northwest from Kakamega in Kenya into Uganda on the northern shore of Lake Victoria. It is located in the Archean Tanzanian craton near the northeastern end of the LVG (Poulsen, 2015) [1]. Most workers in this belt (Poulsen, 2015; Huddlestone, 1954; Pulfrey, 1946) [1, 2, 3]. Established three main stratigraphic divisions in their mapping. These were noted as gneissic basement, Nyanzian volcanic and sedimentary rocks, and Kavirondian sedimentary rocks (Figure 2). Fault zones divide thrusted and folded stratigraphic segments. Regional folding of the belt is witnessed while approaching the Ugandan border. Geochronological study and field correlations have revealed a comprehensive stratum in the region. An Upper Nyanzian package of ultramafic, mafic, and felsic volcanics overlies Lower Nyanzian volcaniclastics/BIFs and mafic volcanics. Younger Kavirondian polymictic conglomerates and sediments overlie the Nyanzian rocks unconformably. Rambi is intruded by post Archean dolerites. It is recorded that most Busia-Kakamega belt rocks exhibit minimal strain at the outcrop size (Henckel et al., 2016; Poulsen, 2015) [4, 1].

An inferred reef was modelled from the 2018 research from georeferenced colonial maps, to assist in further locating the original reef and establish its existence. Ahafo Gold District in Ghana lies on the West-African Archean Craton. The similarity between Ahafo gold district and the Nyanzian/Kavirondian deposit is their structurally controlled lode-gold deposits which often occur in spatial relationship with altered zones, shear zones and zones of lithological discontinuities Vearncombe, (2023) [5]. suggests that early-priority exploration technologies include geophysics and study on structural geology. This has and is being exercised at Ahafo where new exploration techniques, especially geophysical methods, are applied and are helping locate the gold ore deposits.

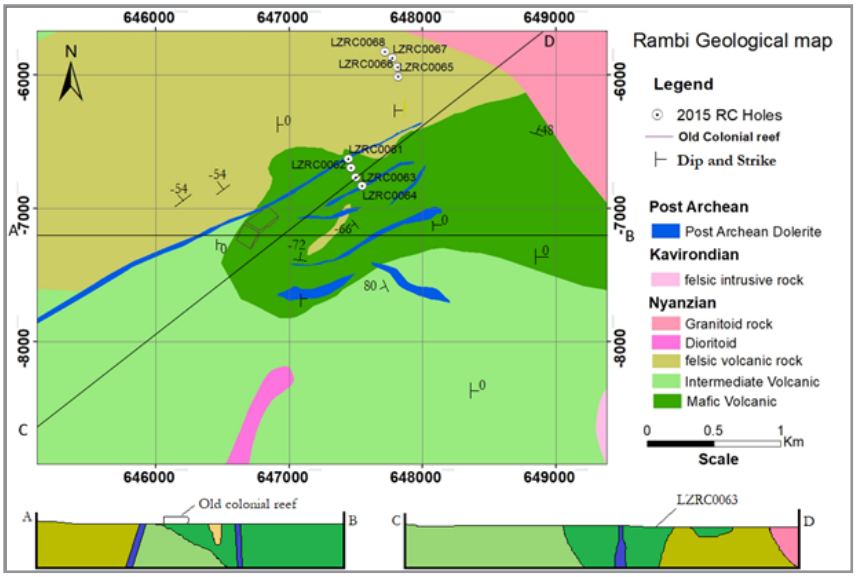

Figure 2: Map Showing Recently Mapped Geology of the Rambi Prospect

At the Rambi target, Reverse Circulation drilling of eight holes was carried out from 2014 to 2015 at the earlier combined Rambi-Aila Target. Rated among the best results were: 1m @ 2.50g/t Au from 34m depth of hole and 1m @ 5.59g/t Au from 105m depth of same hole on the Rambi target. In late 2017, soil sampling confirmed a continuous (> 0.5km) soil anomalies and exposed other unknown areas to be considered for further exploration work.

Methodology and Materials

Different methods were applied to realize the objectives of this project. These included analysis of data from geophysical survey, analysis of different geochemical data and analysis of structural deformation in the prospect.

In 2010, Aviva Corporation Ltd, previously in charge of the prospect, undertook an Airborne Geophysical survey. This led to a detailed acquisition of airborne magnetic, radiometric, and digital terrain survey data which was collected and processed for different targets in western Kenya (Geophysical Report of 2010). The survey including the Rambi Target was flown using the WGS84 coordinate system (a Universal Transverse Mercator projection) derived from the World Geodetic System and was contained within zone 36 with a central meridian of 33 degrees. These datasets underwent the initial basic processing of the raw data. The survey data acquisition specifications are specified in Table 1 below.

Table 1: Showing Airborne Geophysical Survey Specifications.

PROJECT NAME	LINE SPACING	LINE DIRECTION	TIE LINE SPACING	TIE LINE DIRECTION	SENSOR / FLIGHT HEIGHT	TOTAL LINE (KM)
Western Kenya	100m	160-340	1000	070	50m	26,245

Shanta Gold, Kenya Ltd who is now in possession of the data (i.e., magnetic and radiometric data with a sampling rate of 0.1 Seconds (10Hz)) provided these datasets and partly the geochemical data, to enable the project to carry out its studies. According to the research objectives, the needed geochemical and petrographic analysis of particular samples were carried out in this research study. X-Ray Fluorescence (XRF) is an excellent qualitative and quantitative analysis for material composition. The XRF machine used was a Bruker 600N3187 Model used to analyze 8 representative rock samples. It is designed to quickly and accurately report the elemental analysis of samples. The detailed process of analysis and all the results are well documented in the link: (Obindah, Maryce, "Whole-Rock X-Ray Fluorescence Results for altered rock samples from Rambi gold Target Western, Kenya", Mendeley Data, V1, 2025, doi: 10.17632/xf2°8c2586.1).

On the other hand, the X-Ray Diffraction (XRD) was used to determine mineralogical composition of rock samples obtained from the Target. It best used to identify individual minerals, including clays and pyrite, present in rock or soil samples. A total of eight altered representative samples were analyzed at the KenGen X-Ray Diffraction laboratory in Olkaria. The eight samples were prepared for the process by crushing them into fine powder, a method termed, the Powder-Method. Powder-Method is the most efficient method used to identify minerals in samples. Reportedly, this was done by dissolving the powder sample in a test tube half full of distilled water. A few drops of the dispersed sample solutions were then mounted on marked glass slides and left to dry for 24 hours. The remaining sample solutions are glycogenated and heated at 550°C for two hours. The above process and results of the analyzed samples are well explained in the link: (Obindah, Maryce, "X-Ray Diffraction Analysis Results of altered rock samples from Rambi gold target, Western Kenya", Mendeley Data, V1, 2025, doi: 10.17632/g4r2nn2bdw.1. Three representative samples from among the eight were sampled for

Thin _Section analysis. The samples originated from different holes at different depths. The detailed process of preparation and results of the three representative samples are well stipulated in the link: (Obindah, Maryce, "Thin-Section photomicrograph results of Rock samples from Rambi gold Target, Western Kenya", Mendeley Data, V1, 2025 doi: 10.17632/73f7pkkmh8.1). ESRI ArcGIS, Oasis Montaj (Geosoft), Rockworks 17, S1 Remote Ctrl and SI Sync, PowDLL conversion software and EVA assessment software were the softwares used to process data in the whole of this research study.

Results & Discussions

Results from the set objectives show that several tectonic events have occurred at regional and local scales. These events have led to hydrothermal fluid alteration which is evident in the rock's petrographic and geochemical analysis. From aeromagnetic data, major and minor structures in the regional geology were identified and analyzed. Primary images like the Total Magnetic Intensity (TMI) Anomaly map were enhanced to improve the visibility of the structures. Structural analysis of Rambi and its proximal surroundings reveal regional geological movements that have occurred in the region over time. Structural faulting, folding, and shearing effects are evident in the aeromagnetic data acquired of this region (Figure 3).

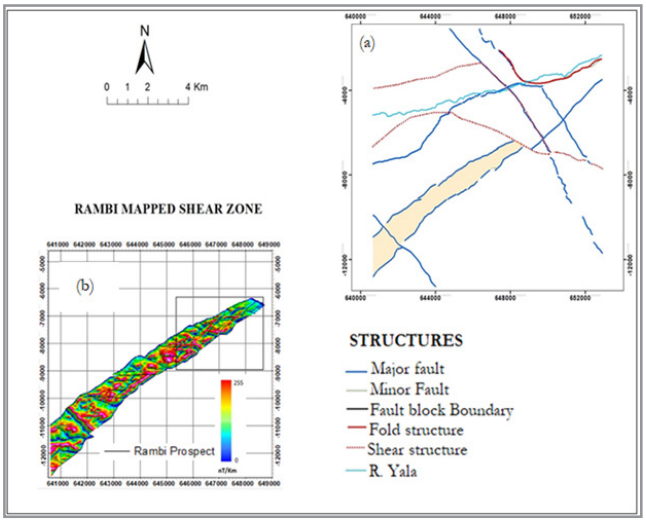

Figure 3: (a) Tilt Angle Derivative (Tad) Image Showing Main Rambi Shear Zone (Yellow Zone) (B) Highlighted Rambi Shear Zone Divided By Minor Fault Structures That Form Fault Blocks

From closer analysis of the Rambi structures, Figure 3(a) shows a generally NW-SE trending strike-slip fault that encloses the prospect from the North and displays a northward shift of Rambi shear zone (yellow-zone) as a whole. This shear is also enclosed by two major bounding faults. Cross-cutting the shear zone are several visible almost E-W trending minor faults that have resulted to the formation of micro-fault blocks Figure 3(b). Closer observation of the fault blocks suggests opposing fault movements between adjacent blocks. According to Mikucki, (1998) and Groves et al., (2018) [6, 7], world-class orogenic gold deposits are frequently found in deformed volcano-sedimentary sequences next to triple-point junctions characterized by regionally scaled zones of micro-block assembly. This might be a likely case for Rambi due to the juxtaposition of the same groups of rocks witnessed in the target and the resultant micro-fault blocks. The general trending direction of the shear in relation to the local trending direction, the cross-cutting faults and the indistinct internal shear zones presents a case similar to the Zuleika shear zone. Located in this shear zone is the renown Kundana Goldfield of Western Australia, that is in active production of major ounces of gold worldwide. Figure 4b displays the structural map of the Zuleika Shear zone.

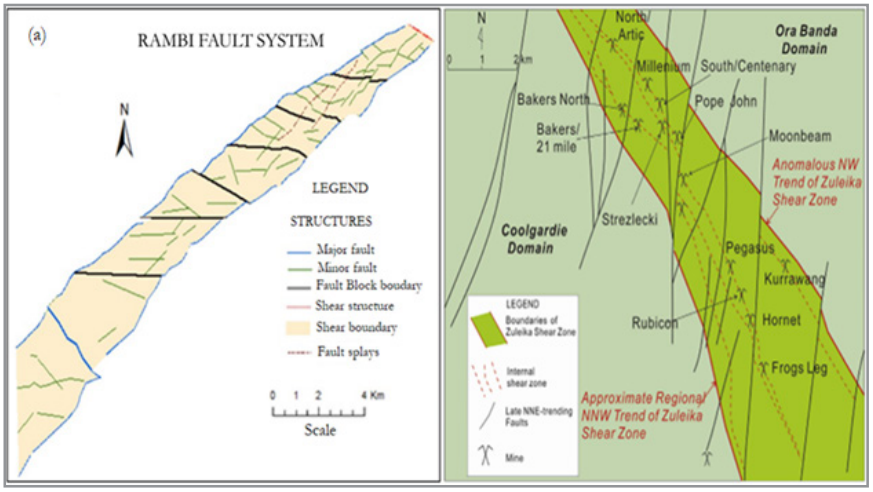

Figure 4: (a) Rambi Fault System Showing the Cross-Cutting Faults and The Internal Shear Zones Vis A Vis (A) The Structures In Kundana Goldfield In Zuleika Shear Zone of Western Australia

Cross-faults are interpreted as accommodation faults (Weinberg et al., 2004) [8]. They are caused by a jog in the Zuleika Shear Zone. This is movement from the regional NNW trend to a local NW trend. Orogenic gold deposits in the Zuleika Shear Zone are majorly located around the junctions of cross-faults in subsidiary/internal shears as evident in Figure 4b. Structurally, this scenario resembles the case with the Rambi shear zone. Both cases exhibit a sense of a general-trend for the main shear and a local trend for the subsidiary shears, which result to cross-faults. The general trend of the shear is in the ENE-WSW direction which classifies as Deformation 1 (D1) structures. Other classes include the D2, D3, and ?D4 structures classified depending on their structural orientation in relation to each other which depicts their time of occurrence.

The fault splays that form the internal or subsidiary shear zones take a local NNE-SSW trend, that classifies under the D3 structures. These potential shears align with the mined colonial "Fabal" reef that measure ~43° strike direction and ~75° dipping NW according to the historical and 2018 drilling information. The splays deviate (deviation from the general to local trend) about 9°-23° (estimated from the Rose Diagram) which closely compares to the Kundana Goldfield. These non-linear sections jog into an unusual direction of 10°-25° to the mean trend. These jogs do allow for orogenic gold ore deposition and accumulation. This vital characteristic witnessed in both cases makes Rambi a target of focus. The mineralized internal shears could be to a depth of ~400m according to prior analyzed data from RC and Diamond drilled samples which have shown us the extent of alteration. Groves et al., (2018) and Weinberg et al., (2004) [6, 7] explain that linear zones of crustal to lithospheric-scale faults and shear zones with the mean structural trend often lack economically significant gold resources. This reasoning could majorly explain why the 2018 Diamond-drilling program did not hit any significant values of gold due to lack of sufficient information of the targets and most potential zones to hit.

Figure 5 below shows target's Figure 5(a)similarity with the Boulder Lefroy shear zone that lies to the east of the Kambalda Anticline in the Yildarn cration while Zuleika shear zone is to the west. The Boulder Lefroy shear conspicuously shows the strong effect of the jogs in the system Figure 5(b). The shear is recognized as a major conduit for gold mineralization in the world-class Kalgoorlie Goldfield that is located within it. The Zuleika shear has a number of other separate historical and current operating mines that have produced to date, ~20M Ounces. The two scenarios point to the need for extensive exploration work that is needed at Rambi to unravel its maximum potential as a prospect.

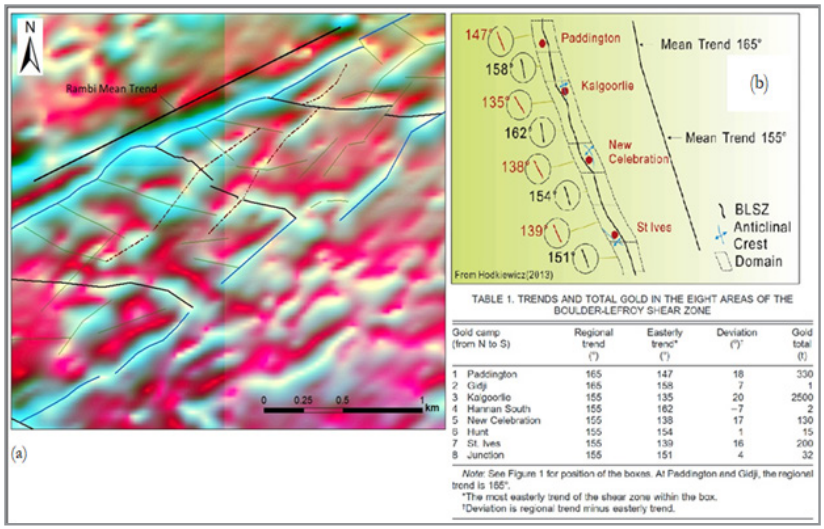

TABLE 1. TRENDS AND TOTAL GOLD IN THE EIGHT AREAS OF THE BOULDER-LEFROY SHEAR ZONE

Gold camp (from N to S)	Regional trend (°)	Easterly trend* (°)	Deviation (°)†	Gold total (t)
1 Paddington	165	147	18	330
2 Gidji	165	158	7	1
3 Kalgoorlie	155	135	20	2500
4 Hannan South	155	162	−7	2
5 New Celebration	155	138	17	130
6 Hunt	155	154	1	15
7 St. Ives	155	139	16	200
8 Junction	155	151	4	32

Note: See Figure 1 for position of the boxes. At Paddington and Gidji, the regional trend is 165°.
*The most easterly trend of the shear zone within the box.
†Deviation is regional trend minus easterly trend.

Figure 5: (a) Analytical Signal (total gradient) Image of Rambi Showing Jogs/Cross-Faults. (b) Boulder-Lefroy Fault, Showing Jogs and Major listed Orogenic Gold Districts Along its Internal Shear Zone

Geochemically, XRD analysis indicate all the samples from Au-potential zones are highly altered. Hydrothermal resultant minerals observed from the samples include calcite, chlorite, illite, and kaolinite. These minerals indicate the presence and the levels of hydrothermal alteration in the target. The gold deposits are thought to have formed by precipitation of gold from hydrothermal fluids transported through the shear zones. The hydrothermal fluids were likely generated by the breakdown of metamorphic rocks in the shear zone. The alteration assemblages reflect a range of fluid and temperature conditions, and they can additionally be used to infer the tectonic setting of the Rambi Shear Zone. For example, carbonate, a younger hydrothermal alteration assemblage, supports younger age of shear zones (Groves et al., 2018) [7]. Most clays are as a result of the weathering of feldspars. This is evident with the observed K-feldspar mineral on photomicrograph of several samples. The higher the amount of clay minerals in rock the higher the levels of hydrothermal alteration interference with the rock. This raises chances of orogenic gold occurrence and formation leading to gold deposition as in the case of Rambi. Table 2 below shows the alteration assemblage minerals after hydrothermal alteration in the rocks.

Table 2: Alteration Mineral Assemblages at Rambi (Mason, 2018)

Parent minerals/Rock	Alteration assemblages
Olivine phenocrysts	Carbonate (calcite)+quartz+ opaques (magnetite, hematite)+ Chlorite

Clinopyroxene phenocrysts	Fine-grained calcite+chlorite+talc
Ti-Magnetite	Leucoxene
Plagioclase phenocrysts	Albite+clinozoisite
Ferromagnesian phenocrysts	Chlorite+clinozoisite
K-Feldspar	illite

Most of Quartz crystals, apatite Cr-spinel (small inclusions in Olivine) and biotite survived. The groundmass was partly altered to calcite+Opaque (hematite, magnetite) +talc .(Referenced from Dog. Mason Lab Report (Partly shared in Appx B))

The Boulder Lefroy and the Zuleika shear zones, display similar hydrothermal alteration mineral assemblages when compared to Rambi. These include a variety of clay minerals, Chlorite, Quartz, and Pyrite. The alteration assemblages at Rambi reflect a range of fluid and temperature conditions in the target. Potential deformed zones at Rambi generated majorly by shearing created weak zones that allow the flow of hydrothermal fluid. These zones can be traced by the presence of gold accompanying mineral assemblages located in several minor shear zones observed at local scale on 2018 Diamond drilling core samples.

Most of the rock samples from the petrographic analysis depict a range of different rock types depending on the silica content. The results relate to similar findings that resulted from sampling a larger number of rocks analyzed by the ICP_Ms geochemical method (Appx. A). These rocks range from the ultramafic to felsic types. Optical petrography of a few samples aided in deducing a conclusive identity of some of the rocks. Example of a rock specimen examined is the sheared ultra-mafic rock illustrated in Figure 6 below.

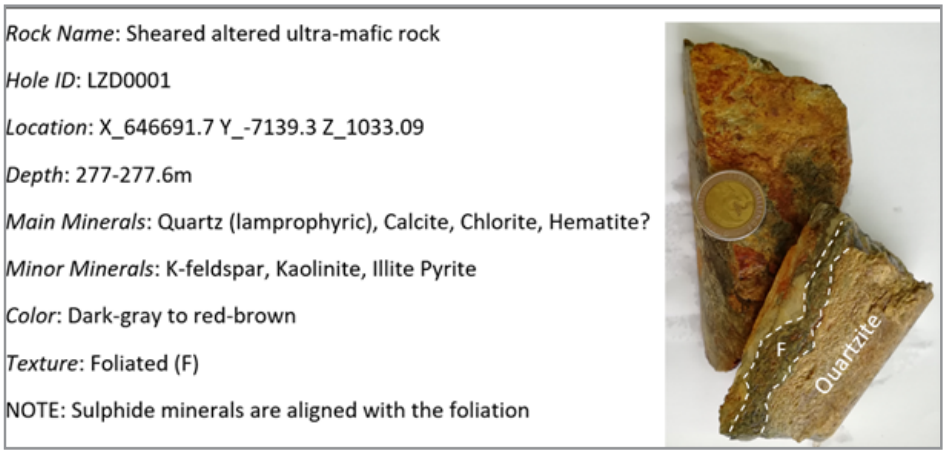

Figure 6: Hand Specimen RAM1382 Showing its Physical Characteristics

The sheared altered ultra-mafic rock shown above is fine-grained in texture. It displays strong pervasive alteration effects, with almost none of the primary minerals observable on the hand specimen due to the high level of alteration. High amounts of quartz were observed especially present in the polished thin-section. Hematite dominated the joints, appearing as red-brown color on the hand specimen due to exposure of the sample to high oxidizing agents. Pyrite occurs as small subhedral grains, aggregates along the foliation planes, and sparsely and irregularly disseminated on the rock.. The foliation effect produced foliation texture on the hand specimen which also appears on the thin section, containing different kinds of altered minerals, as shown in Figure 7.

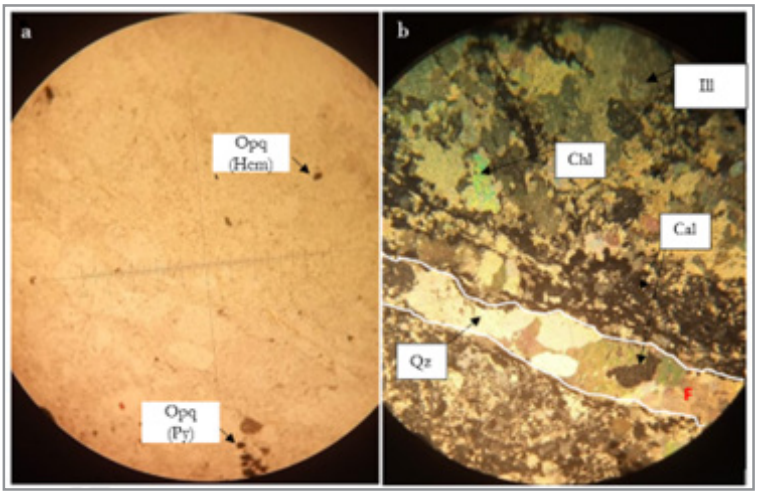

Figure 7: Photomicrograph of Sample RAM1382. (a) Thin Section on PPL Mode. (b) Same Thin Section on XPL. Foliated Texture (F) Appears in Both the Thin-Section and the Hand Specimen. Mag. X60. Chl=Chlorite, Cal=Calcite, Ill=Illite, Qz=Quartz, Py=Pyrite, Hem=Hematite

Figure 8 is an elaborate plot used to classify the broader class of the rocks (from the 52 samples analyzed for ICP_Ms) and suggests different magma types. The Zr/TiO2 ratio is a surrogate for SiO2 and Cr/Al as a variable, allowing for a clear distinction of the Cr-rich rocks from the typical andesite. This classification method has proven to be one of the best representations of the variation in volcanic rock compositions in the Busia-Kakamega belt.

Figure 8 is an elaborate plot used to classify the broader class of the rocks (from the 52 samples analyzed for ICP_Ms) and suggests different magma types. The Zr/TiO2 ratio is a surrogate for

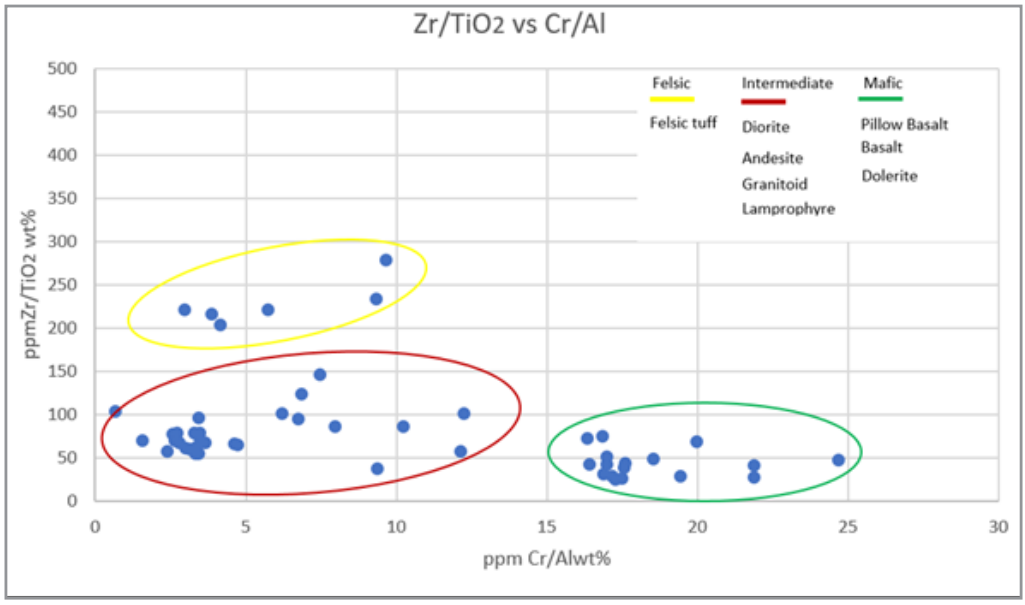

Figure 8: Discriminant Diagram of Rock Types in Rambi Using Zr/Ti and Cr/Al Ratios Distinguishing Three Compositional Volcanic Groups. (Diagram after Poulsen, 2015)

Figure 9 shows gold pathfinder elements as obtained from the whole-rock XRF geochemical analysis. Zn, Ni and As trace elements seem to populate almost all the samples. Mo is the Least occurring. The traces of path-finder elements on all the altered rock samples from varied depths are a good indication of how spread hydrothermal fluid is in the target.

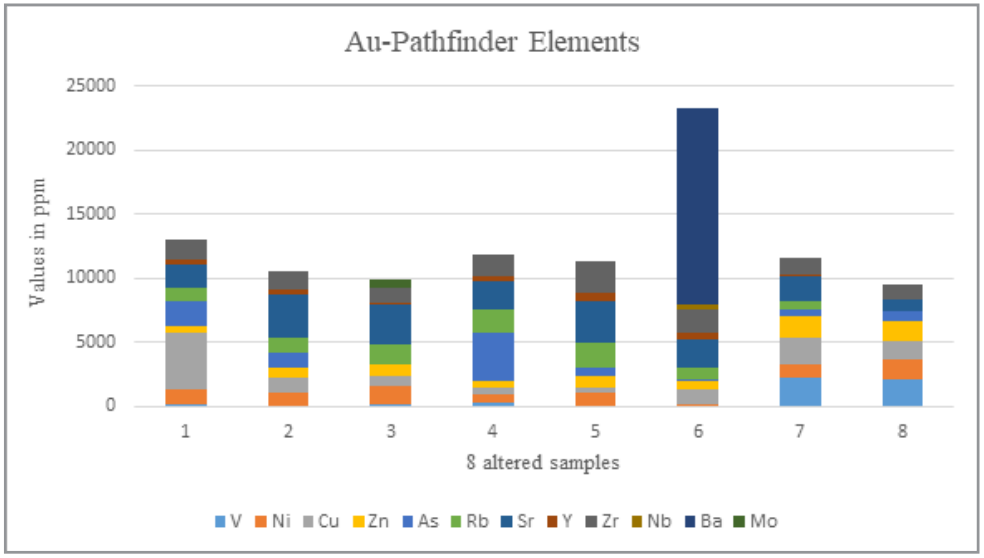

Figure 9: Analyzed Au Pathfinder Elements from XRF Whole-Rock Results from Across 3 wells

The target is deformed by differently oriented fault structures of different magnitudes. Ideally, to this, Mikucki (1998) and Foster and Piper (1993) [9] denote that significant gold-producing terranes have a complicated tectonic history of strike-slip and reverse dip-slip sense of shearing, with rich lodes. These rich lodes are often supported by second (D2) or higher-order structures (D3 and ?D4) that are adjacent to faults and shear zones regarded as first-order structures (D1) on the crustal-scale. These D1 shear zones are a crucial component of late reverse, dip-slip activation or reactivation, which provides the ideal conditions for crustal de-watering during prograde metamorphism and tonalitic magma emplacement. The D1 fault structures as shown in Figure 10(a) could have resulted from thrusting events in the Busia-Kakamega Belt. Due to inferred compressional forces, D2-shortening

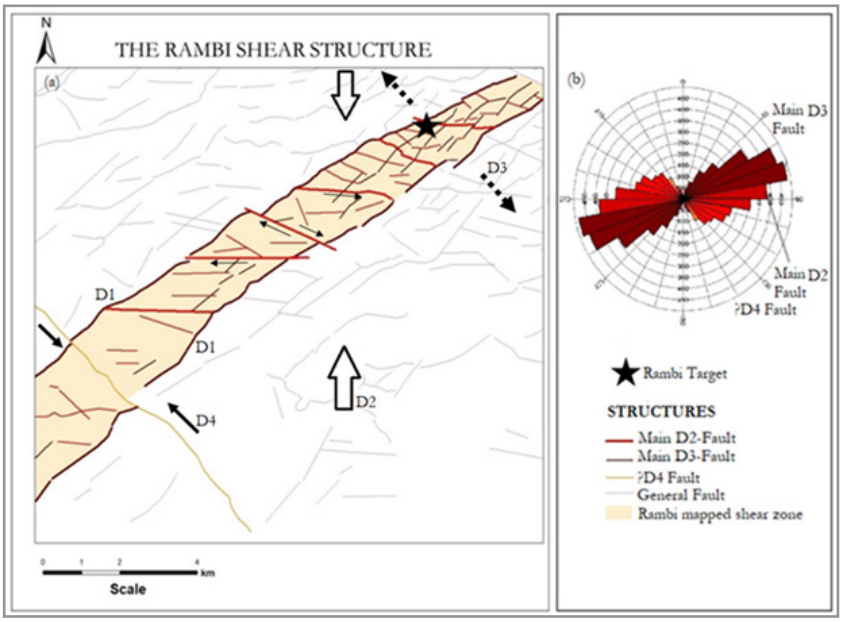

Figure 10: (a) Classified Episodes Of D1, D2, D3 and ?D4 Structures Located Within the Main Rambi Shear Zone. (b) Rose Diagram Showing Two Principal Strike Directions OF Ene-Wsw And Wnw-Ese

Event took place. These led to deactivation of older normal faults and formation of a new series of newly formed (neoformed) faults that came as a result of continued shortening. Minor fault blocks along the main shear were activated moving in relative strike-slip motion to adjacent fault blocks producing dextral offsets. Some of the neoformed faults included a series of ENE-trending faults that include a complex of structures to the far ENE section of the main Rambi shear. This is the section that classifies as highly prospective site for gold in Rambi as a prospect. Part of the ENE-trending faults, are linking faults that are produced during the continued shortening (Miller et al., 2010) [10]. Internal shear zones form part of the linking minor faults that form contractional jogs for gold accumulation. These structures are also inferred to control location of mafic dolerite units (post-archean dykes) D3 NW-SE extensional episode led to the dykes overprinting most of the D2 faults. The shear zone and fault structures (D2 and D3 structures) as clearly shown from the Rose Diagram below, have been regarded as open and permeable to promote and channel the passage of a significant volume of hydrothermal fluids across the orogenic gold hydrothermal system, from source areas to trap zones at the regional scale (Boadi et al., 2022) [11]. ?D4 fault is another singular set of dextral faults and the major far field applied stress is inferred to have been SE-NW tensional forces.

The strike directions of the D2 and D3 faults in the Rambi shear zone revealed two principal strike orientations (Figure 10b) for all the structures around and within the main ENE-WSW shear zone. They slightly cut across each other (9°-23°), most of them creating cross-joints/jogs that form good sites for ore deposition. From observations from the prior investigations for gold in the study area, all the other structures deem prospective apart from the original D1 that could have acted as hydrothermal fluid conduits which hand less priority.

Conclusion

The Rambi fault system suggest four deformational phases in the region that have led to differently oriented fault structures. These deformational phases suggest a sign of different episodes of deformation occurring over the study area. The colonial "Fabal" reef classifies into the D3 faults and strikes NE-SW dipping to the NW (from populated data of the 3D construction of the colonial mine and the 2018 data collected (Average foliation=280°) (Nandeche and Koech, 2018). This suggests of high possibility of the newly inferred internal shear structures also dipping to the NW direction. The colonialists having described the mineralization environment as "a 5m gold-quartz vein within a shear zone" raises confidence and viability of the newly mapped internal shear zones. For mineralization to take place, the presence of porous rocks, e.g., tuffs, basalt (pillow basalt), andesite, allowed for the flow of the hydrothermal fluid (Figure 11). The general mineral assemblages (carbonate (calcite) and chlorite) realized from the XRD and thin-section analysis indicate a low-grade regional metamorphism of greenschist facies as similarly concluded by many authors including Groves et al. (2018) and Mason (2018) [12].

The identification of the inferred potential internal shears (Weinberg et al., 2004) [7] within main Rambi ,shear was one of the greatest achievements. The two or more of the potential internal/subsidiary shear zones are potential sites for investigation of lode gold ore deposit seated within the main Rambi shear. To add to the findings, the strike direction of the upper internal shear zone directly aligns with the location of the historically inferred colonial reef that gave 3175 Ounces of gold between 1930 to 1960. Their slight deviation from the general trend offers potential sites for gold mineralization as observed from similar gold potential sites.

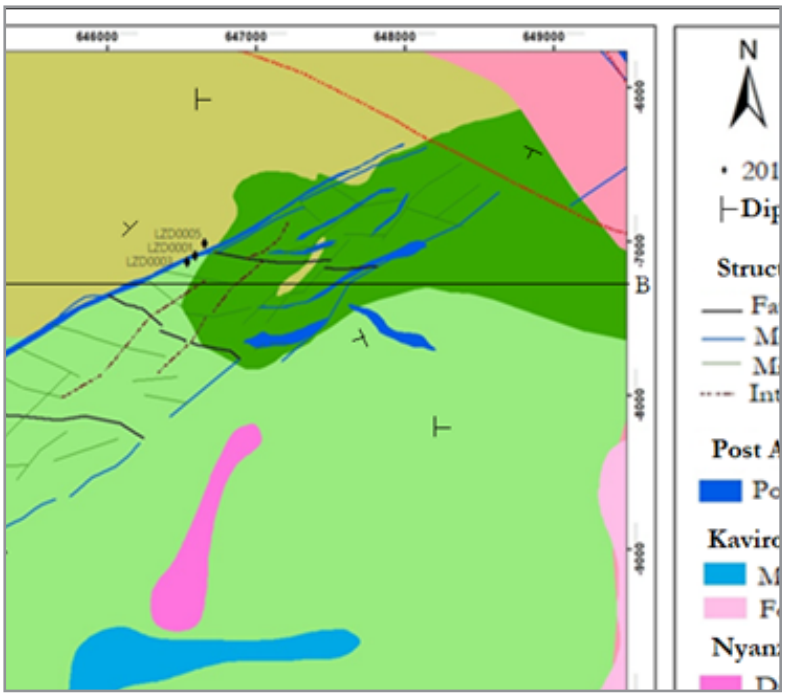

Figure 11: Geology of Rambi Target with Integrated Mapped Prospective Internal Shears

The Boulder Lefroy and the Zuleika shear zones within the Yilgarn Craton of Western Australia are recorded to have an almost similar tectonic setting. They are located in collisional orogens, extensional basins, and transtentional? zones. Similarity of these potential targets in comparison to Rambi is as shown in Table 3.

Table 3: Similarities of Rambi With Other Gold-Related Shear Zones

Geology	Boulder Lefroy shear zone	Zuleika Shear zone	Rambi Shear zone
Structural setting	Internal shear zone with jogs/ cross faults	Internal shear zone with jogs/ cross faults	Internal shear zone with jogs/ cross faults
Alteration mineral assemblage	Sericite Chlorite Quartz Pyrite	Sericite Chlorite Quartz Pyrite	Sericite Chlorite Quartz Pyrite Albite Carbonate *pyrhotite
Deformation zones	Collisional orogens, Extensional basin, transtensional zones	Collisional orogens, Extensional basin, transtensional zones	Collisional orogens, Extensional basin, ?transtensional zones

Acknowledgement

The authors are grateful for the assistance offered by Shanta Gold, Kenya led by Cris Sang', the Exploration Manager, for freely offering data needful for the research study. A heartfelt acknowledgement to my supervisors (mentioned on the Title Page), Dr. Waswa and Prof. Dindi, Structural Geologists in the Earths and Climate Department, UON whose advice and opinion added to the research. Geologist Godwin Mzumbi from the Ministry of Mining, Blue Economy and Maritime Affairs for his geophysical expertise. Mr. Mbiga, a Technician from the Earths and Climate Department, UON whose expertise in the laboratory led to great findings [13-16].

References

1. Henckel, J., Poulsen, K. H., Sharp, T., & Spora, P. (2016). Lake victoria goldfields. Episodes Journal of International Geoscience, 39(2), 135-154.
2. Huddlestone, A. (1954). Geology of the Kakamega district. Colony and Protectorate of Kenya Geological Survey of Kenya, Government Printer Nairobi.
3. Huddlestone, A. (1954). Geology of the Kakamega district. Colony and Protectorate of Kenya Geological Survey of Kenya, Government Printer Nairobi.
4. Henckel, J., Poulsen, K. H., Sharp, T., & Spora, P. (2016). Lake Victoria Goldfields. Episodes, 39(2), 135–154.
5. Vearncombe, J. R. (2023). Function and status of structural geology in the resource industry. Australian Journal of Earth Sciences, 70(6), 908–931.
6. Mikucki, E. J. (1998). Hydrothermal transport and depositional processes in Archaean lode gold systems: A review. Ore Geology Reviews, 13(4–5), 307–321.
7. Groves, D. I., Santosh, M., Goldfarb, R. J., & Zhang, L. (2018). Structural geometry of orogenic gold deposits: Implications for exploration of world-class and giant deposits.

1. Geoscience Frontiers, 9(4), 1163–1177.
2. Weinberg, R. F., Hodkiewicz, P. F., & Groves, D. I. (2004). What controls gold distribution in Archean terranes? Geology, 32(7), 545–548.
3. Foster, R. P., & Piper, D. P. (1993). Archaean lode gold deposits in Africa: Crustal setting, metallogenesis and cratonization. Ore Geology Reviews, 8(4), 303–347.
4. Miller, J., Blewett, R., Tunjic, J., & Connors, K. (2010). The role of early formed structures on the development of the world-class St Ives Goldfield, Yilgarn, WA. Precambrian Research, 183(2), 292–315.
5. Boadi, B., Sunder Raju, P. V., & Wemegah, D. D. (2022). Analysing multi-index overlay and fuzzy logic models for lode-gold prospectivity mapping in the Ahafo gold district, southwestern Ghana. Ore Geology Reviews, 148, 105059.
6. Mason, D. R. (n.d.). Petrographic descriptions for drill core rock samples from drill hole LZD0001 (Rambi Prospect) and LZD0002 (Ramba Prospect), Kenya (Petrographic Report 4243, 25 p.). Mason Geoscience Pty Ltd. Available at Shanta Gold Exploration Kenya Ltd Library.
7. Obindah, M. (2025). X-ray diffraction analysis results of altered rock samples from Rambi gold target, Western Kenya [Data set]. Mendeley Data, V1. https://doi.org/10.17632/g4r2nn2bdw.1
8. Obindah, M. (2025). Whole-rock X-ray fluorescence results for altered rock samples from Rambi gold target, Western Kenya [Data set]. Mendeley Data, V1. https://doi.org/10.17632/xf208c2586.1
9. Obindah, M. (2025). Thin-section photomicrograph results of rock samples from Rambi gold target, Western Kenya [Data set]. Mendeley Data, V1. https://doi.org/10.17632/73f7pkkmh8.1
10. Nandeche, M., & Koech, W. (n.d.). Rambi Technical Completion Report (Unpublished manuscript, 32 p.). Archived at Shanta Gold Kenya Library.

Appendix A: Analyzed Geochemical Results from ICP_MS61

	Std Oxide conversion factors	DDA35651	Oxide	DDA35652	Oxide	DDA35653	Oxide	DDA35654	Oxide	DDA35655	Oxide	DDA35656	Oxide	DDA30332	Oxide	DDA30338	Oxide	DDA30353	Oxide
Al_ME-MS61_pct	1.8895	7.53	14.227935	7.1	13.41545	7.65	14.45468	7.62	14.39799	6.99	13.20761	7.35	13.88783	6.71	12.67855	5.92	11.18584	7.83	14.79479
Ca_ME-MS61_pct	1.3992	4.78	6.688176	4.54	6.352368	4.3	6.01656	2.32	3.246144	3.89	5.442888	7.31	10.22815	7.6	10.63392	5.46	7.639632	11.35	15.88092
Fe_ME-MS61_pct	1	7.53	7.53	7.48	7.48	7.02	7.02	6.29	6.29	3.45	3.45	9.8	9.8	8.9	8.9	2.18	2.18	7.65	7.65
K_ME-MS61_pct	1.2046	0.03	0.036138	0.28	0.337288	0.56	0.674576	0.05	0.06023	2.07	2.493522	0.03	0.036138	0.8	0.96368	3.14	3.782444	2.62	3.156052
Mg_ME-MS61_pct	1.6582	1.74	2.885268	1.82	3.017924	1.99	3.299818	1.63	2.702866	0.73	1.210486	3.65	6.05243	3.21	5.322822	0.42	0.696444	2.12	3.515384
Na_ME-MS61_pct	1.348	2.61	3.51828	2.03	2.73644	3.03	4.08444	3.78	5.09544	0.96	1.29408	1.04	1.40192	0.23	0.31004	0.16	0.21568	0.11	0.14828
S_ME-MS61_pct	2.4972	0.02	0.049944	0.02	0.049944	0.01	0.024972	0.01	0.024972	1.5	3.7458	0.06	0.149832	0.19	0.474468	0.6	1.49832	1.87	4.669764
Ti_ME-MS61_pct	1.6681	0.762	1.2710922	0.786	1.3111266	0.656	1.094274	0.681	1.135976	0.36	0.600516	0.722	1.204368	0.616	1.027755	0.253	0.422029	0.527	0.879089
Total			36.206833		34.700541		36.66931		32.95362		31.4449		42.76067		40.31102		27.62039		50.69427
NOTE: The geochemical method of analysis (ICP_MS61) selected by Shanta does not involve the analysis of Silicon (Si) element																			
Ag_ME-MS61_ppm		0.07		0.02		0.08		0.02		0.33		0.03		0.05		0.03		0.24	
As_ME-MS61_ppm		18		14.5		14.7		9.8		16.5		4.6		43.9		26.8		93.7	
Ba_ME-MS61_ppm		90		90		160		40		410		10		60		270		220	
Be_ME-MS61_ppm		0.49		0.54		0.52		0.57		1.02		0.49		0.33		0.49		1.42	
Bi_ME-MS61_ppm		0.04		0.02		0.03		0.005		0.23		0.01		0.04		0.02		0.09	
Cd_ME-MS61_ppm		0.09		0.14		0.12		0.1		3.1		0.13		0.11		0.1		0.07	
Ce_ME-MS61_ppm		24.2		24.6		21		32.1		28.4		12.2		10.3		14.05		22.7	
Co_ME-MS61_ppm		36.7		36		36.2		24.4		31.3		52.8		50.1		14.8		45.5	
Cr_ME-MS61_ppm		18		11		28		5		27		125		116		34		80	
Cs_ME-MS61_ppm		0.4		1.32		1.29		0.35		7.5		0.49		1.89		2.8		5.99	
Cu_ME-MS61_ppm		80.8		75.7		58.8		37		261		84.3		96.1		43.1		25.4	
Ga_ME-MS61_ppm		20		18.65		19.55		19.8		19.15		19.05		16.6		17.6		19.5	
Ge_ME-MS61_ppm		0.14		0.12		0.12		0.13		0.13		0.11		0.11		0.12		0.13	
Hf_ME-MS61_ppm		1.9		2.6		1.9		2.8		3.2		1.7		0.8		2.4		1.9	
In_ME-MS61_ppm		0.07		0.078		0.06		0.09		0.182		0.091		0.084		0.027		0.086	
La_ME-MS61_ppm		10.7		10.9		9.3		14.9		13.5		4.6		3.9		6.4		10.9	
Li_ME-MS61_ppm		21.1		32.5		27.5		26.4		14.9		14.1		44.9		5.3		32.3	
Mn_ME-MS61_ppm		1010		916		939		836		614		1420		1410		687		1720	
Mo_ME-MS61_ppm		1.02		0.83		0.77		0.93		2.11		0.61		0.29		0.9		1.45	
Nb_ME-MS61_ppm		4.8		5.1		4.1		5.9		5		3.6		3		3.5		3.3	
Ni_ME-MS61_ppm		44.6		38		53.9		9.3		40.5		110.5		103.5		28.8		94.3	
P_ME-MS61_ppm		630		640		510		780		490		450		390		320		610	
Pb_ME-MS61_ppm		4.6		4.1		3.4		2.8		8.4		3		1.6		2.1		4	
Rb_ME-MS61_ppm		0.8		10.7		19.8		1.2		62.5		0.6		32.1		88.1		100	
Re_ME-MS61_ppm		0.006		0.005		0.006		0.005		0.005		0.008		0.005		0.004		0.006	
Sb_ME-MS61_ppm		0.71		0.9		0.27		0.25		1.33		0.66		0.77		0.61		1.66	
Sc_ME-MS61_ppm		26.1		25.8		23.8		15.8		12.7		42.9		38.1		9.9		34.6	
Se_ME-MS61_ppm		1		1		0.5		0.5		2		1		1		0.5		1	
Sn_ME-MS61_ppm		1.6		1.2		1.8		0.9		2.7		0.9		0.9		1.1		1.1	
Sr_ME-MS61_ppm		210		148.5		231		99.9		78.9		160		79		60.2		109	
Ta_ME-MS61_ppm		0.34		0.39		0.3		0.42		0.43		0.24		0.19		0.31		0.23	
Te_ME-MS61_ppm		0.025		0.025		0.025		0.025		0.54		0.025		0.025		0.025		0.12	
Th_ME-MS61_ppm		1.17		1.3		0.96		1.44		2.73		0.33		0.26		1.28		0.87	
Tl_ME-MS61_ppm		0.01		0.07		0.11		0.02		0.42		0.01		0.12		0.42		0.36	
U_ME-MS61_ppm		0.3		0.4		0.3		0.4		0.8		0.1		0.1		0.7		1.2	
V_ME-MS61_ppm		188		176		155		108		74		279		252		72		206	
W_ME-MS61_ppm		0.2		0.3		0.2		0.2		1.3		0.1		0.4		4.6		13.6	
Y_ME-MS61_ppm		23.7		23.7		20.9		18.2		13.8		28.3		16.1		8.1		19.6	
Zn_ME-MS61_ppm		99		132		111		117		604		123		96		33		95	
Zr_ME-MS61_ppm		73.4		92.5		73.9		118		129.5		62.2		25.3		93.6		76	
Au_ppm_d														0.01		0.04		0.12	
Au_ppmName_d														Au_AU-AA26_ppm		Au_AU-AA26_ppm		Au_AU-AA26_ppm	

	Std Oxide conversion factors	DDA30361	Oxide	DDA35658	Oxide	DDA30382	Oxide	DDA35659	Oxide	DDA30413	Oxide	DDA30425	Oxide	DDA30431	Oxide	DDA35660	Oxide	DDA30442	Oxide
Al_ME-MS61_pct	1.8895	7	13.2265	8.23	15.550585	2.62	4.95049	7.67	14.49247	7.07	13.35877	5.08	9.59866	7.17	13.54772	6.88	12.99976	5.91	11.16695
Ca_ME-MS61_pct	1.3992	6.68	9.346656	4.73	6.618216	13.75	19.239	4.42	6.184464	3.95	5.52684	7.38	10.326096	7.86	10.99771	8.38	11.725296	8.31	11.62735
Fe_ME-MS61_pct	1	7.88	7.88	6.17	6.17	5.92	5.92	7.2	7.2	4.72	4.72	4.46	4.46	8.44	8.44	9.16	9.16	7.59	7.59
K_ME-MS61_pct	1.2046	1.11	1.337106	0.12	0.144552	0.66	0.795036	0.43	0.517978	3.15	3.79449	1.86	2.240556	0.05	0.06023	0.04	0.048184	2.76	3.324696
Mg_ME-MS61_pct	1.6582	3.24	5.372568	2.37	3.929934	5.62	9.319084	1.96	3.250072	1.21	2.006422	1.4	2.32148	2.08	3.449056	2.96	4.908272	2.88	4.775616
Na_ME-MS61_pct	1.348	0.13	0.17524	2.94	3.96312	0.02	0.02696	2.42	3.26216	0.11	0.14828	1.06	1.42888	2.25	3.033	1.43	1.92764	0.13	0.17524
S_ME-MS61_pct	2.4972	0.09	0.224748	0.03	0.074916	2.61	6.517692	0.03	0.074916	0.07	0.174804	2.07	5.169204	0.16	0.399552	0.27	0.674244	2.41	6.018252
Ti_ME-MS61_pct	1.6681	0.538	0.897438	0.504	0.8407224	0.213	0.355305	0.683	1.139312	0.415	0.692262	0.24	0.400344	0.698	1.164334	0.736	1.2277216	0.614	1.024213
Total			38.46026		37.292045		47.12357		36.12137		30.42186		35.94522		41.0916		42.671118		45.70231
NOTE: The geochemical method of analysis (ICP_MS61) selected by Shanta does not involve the analysis of Silicon (Si) element																			
Ag_ME-MS61_ppm		0.03		0.02		0.91		0.02		0.41		0.76		0.08		0.03		0.38	
As_ME-MS61_ppm		22.9		3		64.9		2.8		26.9		63.1		7.8		2.3		44	
Ba_ME-MS61_ppm		140		110		300		80		490		210		30		20		90	
Be_ME-MS61_ppm		0.31		0.46		0.4		0.52		0.89		1.61		0.3		0.35		1.44	
Bi_ME-MS61_ppm		0.02		0.01		0.005		0.03		0.12		0.39		0.005		0.005		0.005	
Cd_ME-MS61_ppm		0.06		0.06		0.11		0.1		0.12		3.42		0.13		0.23		0.13	
Ce_ME-MS61_ppm		14.5		22.5		13.9		21.4		31.6		39.1		11.35		12.75		9.83	
Co_ME-MS61_ppm		44.3		36.2		30.3		35.8		23.6		39.6		49.4		48.2		49.7	
Cr_ME-MS61_ppm		85		39		9		23		21		49		123		113		104	
Cs_ME-MS61_ppm		1.33		0.79		2.33		1.77		10.75		3.84		0.68		0.44		11.45	
Cu_ME-MS61_ppm		62.5		34.3		38.2		53.2		159		236		86.9		105		63.4	
Ga_ME-MS61_ppm		16.2		19.6		7.14		19.5		19.45		15.35		17.65		19.1		16.05	
Ge_ME-MS61_ppm		0.11		0.1		0.06		0.1		0.13		0.11		0.07		0.07		0.09	
Hf_ME-MS61_ppm		1.4		1.2		0.9		1.9		3.9		2.8		1.2		1.7		1.4	
In_ME-MS61_ppm		0.065		0.053		0.057		0.066		0.087		0.12		0.079		0.088		0.068	
La_ME-MS61_ppm		6.1		9.5		6.5		9.4		15.5		19.4		4.2		4.8		3.6	
Li_ME-MS61_ppm		40.9		21.5		17.2		25.5		21.9		13.5		20.5		12.9		7.6	
Mn_ME-MS61_ppm		1300		930		2130		958		657		961		1490		1430		1240	
Mo_ME-MS61_ppm		0.41		0.95		1.65		0.82		0.9		38.7		0.33		0.68		1.85	
Nb_ME-MS61_ppm		3		3.8		1.4		4.2		5.1		5		3.5		3.9		3.3	
Ni_ME-MS61_ppm		98.4		61.7		31.2		48.9		28.4		54.7		102		81.7		70.3	
P_ME-MS61_ppm		460		670		190		530		650		650		450		490		430	
Pb_ME-MS61_ppm		1.4		2.2		9.5		2.2		4.3		8		2.2		1.9		8.7	
Rb_ME-MS61_ppm		41.9		1.5		20.7		13.7		127		72		1.6		0.7		86.6	
Re_ME-MS61_ppm		0.008		0.005		0.004		0.006		0.003		0.006		0.006		0.007		0.008	
Sb_ME-MS61_ppm		0.33		0.19		1.56		0.52		1.2		3.14		0.42		0.16		2.14	
Sc_ME-MS61_ppm		33.7		22		8.5		25		15.6		11		40		41.1		38.8	
Se_ME-MS61_ppm		1		0.5		1		0.5		2		3		0.5		1		0.5	
Sn_ME-MS61_ppm		0.8		0.9		0.5		1.1		2.2		3.4		0.9		1		0.6	
Sr_ME-MS61_ppm		56.1		248		51.8		193.5		35.3		156		169.5		158.5		134	
Ta_ME-MS61_ppm		0.2		0.26		0.1		0.31		0.43		0.3		0.23		0.25		0.21	
Te_ME-MS61_ppm		0.025		0.025		0.025		0.025		0.25		0.43		0.025		0.025		0.025	
Th_ME-MS61_ppm		0.51		0.76		0.41		1.02		3		6.92		0.29		0.35		0.67	
Tl_ME-MS61_ppm		0.12		0.03		0.11		0.08		0.43		0.32		0.02		0.02		0.46	
U_ME-MS61_ppm		0.5		0.2		0.7		0.3		1.2		2.1		0.2		0.1		0.5	
V_ME-MS61_ppm		204		167		63		168		82		97		280		277		251	
W_ME-MS61_ppm		0.1		0.2		1.7		0.1		2.2		8.5		0.7		0.1		2.2	
Y_ME-MS61_ppm		11.6		11.9		16		20.4		19		15		25.6		29.3		16.1	
Zn_ME-MS61_ppm		88		98		47		110		142		332		119		110		57	
Zr_ME-MS61_ppm		52		54.3		34.3		69.9		153.5		111.5		34		52.3		44.4	
Au_ppm_d		0.01				0.11				0.02		0.13		0.01				0.11	
Au_ppmName_d		Au_AU-AA26_ppm				Au_AU-AA26_ppm				Au_AU-AA26_ppm		Au_AU-AA26_ppm		Au_AU-AA26_ppm				Au_AU-AA26_ppm	

	Std Oxide conversion factors	DDA35661	Oxide	DDA35662	Oxide	DDA35663	Oxide	DDA30460	Oxide	DDA30474	Oxide	DDA35664	Oxide	DDA30480	Oxide	DDA30484	Oxide	DDA30488	Oxide
Al_ME-MS61_pct	1.8895	7.47	14.11457	0.32	0.60464	7.13	13.47214	8.01	15.1349	7.47	14.11457	7.57	14.303515	7.46	14.09567	5.88	11.11026	6.32	11.94164
Ca_ME-MS61_pct	1.3992	8	11.1936	29	40.5768	6.27	8.772984	1.57	2.196744	3.77	5.274984	4.64	6.492288	5.21	7.289832	5.88	8.227296	6.76	9.458592
Fe_ME-MS61_pct	1	9.07	9.07	2.59	2.59	9.61	9.61	6.74	6.74	3.98	3.98	7.13	7.13	7.3	7.3	5.36	5.36	5.63	5.63
K_ME-MS61_pct	1.2046	0.05	0.06023	0.005	0.006023	0.02	0.024092	0.38	0.457748	2.61	3.144006	0.09	0.108414	1.03	1.240738	2	2.4092	2.19	2.638074
Mg_ME-MS61_pct	1.6582	2.66	4.410812	4.4	7.29608	3.84	6.367488	2.45	4.06259	1.07	1.774274	2.06	3.415892	2.15	3.56513	1.12	1.857184	2.17	3.598294
Na_ME-MS61_pct	1.348	2.14	2.88472	0.005	0.00674	0.8	1.0784	2.18	2.93864	0.43	0.57964	2.74	3.69352	1.5	2.022	0.09	0.12132	0.39	0.52572
S_ME-MS61_pct	2.4972	0.12	0.299664	0.13	0.324636	0.11	0.274692	0.02	0.049944	0.54	1.348488	0.01	0.024972	0.17	0.424524	0.01	0.024972	0.82	2.047704
Ti_ME-MS61_pct	1.6681	0.779	1.29945	0.024	0.0400344	0.711	1.186019	0.543	0.905778	0.381	0.635546	0.669	1.115959	0.669	1.115959	0.493	0.822373	0.53	0.884093
Total			43.33304		51.444953		40.78581		32.48634		30.8515		36.28456		37.05385		29.93261		36.72412
NOTE: The geochemical method of analysis (ICP_MS61) selected by Shanta does not involve the analysis of Silicon (Si) element																			
Ag_ME-MS61_ppm		0.02		0.02		0.04		0.05		0.19		0.02		0.07		0.11		0.15	
As_ME-MS61_ppm		7.7		2.3		1.3		3.3		57.8		6.2		5.3		54.9		28	
Ba_ME-MS61_ppm		30		10		10		110		600		60		210		340		270	
Be_ME-MS61_ppm		0.42		0.16		0.29		0.44		0.68		0.5		0.42		0.96		0.51	
Bi_ME-MS61_ppm		0.005		0.005		0.01		0.01		0.14		0.02		0.2		0.01		0.01	
Cd_ME-MS61_ppm		0.08		0.12		0.1		0.08		0.73		0.09		0.08		0.06		0.11	
Ce_ME-MS61_ppm		13.8		2.12		11.85		26.8		29		23.7		20.7		19.75		17.25	
Co_ME-MS61_ppm		45.9		2.1		47.4		33.3		23		34.1		36.4		26.5		34.4	
Cr_ME-MS61_ppm		126		3		120		54		31		20		20		72		22	
Cs_ME-MS61_ppm		1.03		0.06		0.87		1.47		3.95		0.57		1.66		10.05		6.08	
Cu_ME-MS61_ppm		46.3		7.2		63.2		39.1		122		43.4		63.4		34.1		32.1	
Ga_ME-MS61_ppm		19.7		0.79		18.9		17.7		20.2		19.8		19.5		17.25		16.35	
Ge_ME-MS61_ppm		0.07		0.05		0.1		0.09		0.11		0.1		0.06		0.12		0.11	
Hf_ME-MS61_ppm		1.5		0.05		1.5		1.8		3.2		2.2		2.3		2.4		1.8	
In_ME-MS61_ppm		0.126		0.02		0.1		0.055		0.085		0.062		0.066		0.06		0.049	
La_ME-MS61_ppm		5.1		1.1		4.3		11.8		13.7		10.6		8.9		8.6		6.9	
Li_ME-MS61_ppm		20.4		4.3		22.9		38.3		18.8		32.2		38.4		24.1		13.2	
Mn_ME-MS61_ppm		1430		2050		1290		556		767		911		1050		877		1000	
Mo_ME-MS61_ppm		0.3		0.12		0.34		0.59		1.22		0.8		0.85		5.36		5.93	
Nb_ME-MS61_ppm		4.1		0.1		3.5		4.8		4.8		4.3		4.3		4		3.6	
Ni_ME-MS61_ppm		93		0.1		96.3		80.6		36.5		47.4		44.6		38.5		31.7	
P_ME-MS61_ppm		530		30		440		850		460		550		560		500		490	
Pb_ME-MS61_ppm		1.4		2.4		2.3		3.1		4.9		2.3		1.6		2.2		2.3	
Rb_ME-MS61_ppm		1.6		0.2		0.7		12.2		80.9		2.3		39		75.2		77.8	
Re_ME-MS61_ppm		0.007		0.004		0.007		0.006		0.005		0.005		0.005		0.005		0.007	
Sb_ME-MS61_ppm		0.56		0.21		0.16		0.46		1.66		0.42		0.55		1.37		1.16	
Sc_ME-MS61_ppm		45.5		1.6		41.6		21.6		13		24.9		22.8		17.9		19	
Se_ME-MS61_ppm		1		1		1		1		1		0.5		1		1		0.5	
Sn_ME-MS61_ppm		1.1		0.1		1		1.1		1.9		1.1		1		1.1		1	
Sr_ME-MS61_ppm		104.5		303		137		169.5		74.6		192		111.5		87.5		125	
Ta_ME-MS61_ppm		0.28		0.025		0.24		0.32		0.41		0.34		0.31		0.25		0.25	
Te_ME-MS61_ppm		0.025		0.025		0.025		0.025		0.2		0.025		0.025		0.025		0.025	
Th_ME-MS61_ppm		0.34		0.02		0.32		0.93		2.08		1.13		1		2.77		0.88	
Tl_ME-MS61_ppm		0.03		0.01		0.01		0.06		0.43		0.03		0.14		0.25		0.34	
U_ME-MS61_ppm		0.1		0.05		0.1		0.3		0.7		0.3		0.3		0.6		0.6	
V_ME-MS61_ppm		305		13		282		153		86		163		162		144		132	
W_ME-MS61_ppm		0.6		0.2		0.1		0.1		0.6		0.2		0.7		5		4.1	
Y_ME-MS61_ppm		32.3		6.6		28		13.6		11.2		22.7		14.4		12.2		13.4	
Zn_ME-MS61_ppm		100		22		109		105		287		105		84		69		55	
Zr_ME-MS61_ppm		40.9		1.5		89.4		86.4		129.5		77.9		87.2		83.8		69.2	
Au_ppm_d								0.01		0.01				0.01				0.02	
Au_ppmName_d								Au_AU-AA26_ppm		Au_AU-AA26_ppm				Au_AU-AA26_ppm		Au_AU-AA26_ppm		Au_AU-AA26_ppm	

	Std Oxide conversion factors	DDA35666	Oxide	DDA35667	Oxide	DDA35668	Oxide	DDA30502	Oxide	DDA30509	Oxide	DDA30518	Oxide	DDA30524	Oxide	DDA35669	Oxide	DDA35670	Oxide
Al_ME-MS61_pct	1.8895	7.83	14.79479	7.71	14.56805	6.99	13.20761	7.04	13.30208	4.03	7.614685	7.36	13.90672	6.37	12.03612	6.98	13.18871	6.62	12.50844
Ca_ME-MS61_pct	1.3992	5.49	7.681608	4.92	6.884064	4.32	6.044544	5.15	7.20588	8.24	11.52941	6.21	8.689032	5.89	8.241288	4.8	6.71616	4.54	6.352368
Fe_ME-MS61_pct	1	7.19	7.19	6.88	6.88	6.37	6.37	6.81	6.81	6.28	6.28	5.87	5.87	4.47	4.47	6.62	6.62	7.06	7.06
K_ME-MS61_pct	1.2046	0.08	0.096368	0.86	1.035956	0.69	0.831174	0.45	0.54207	1.63	1.963498	3.25	3.91495	2.61	3.144006	0.02	0.024092	0.43	0.517971
Mg_ME-MS61_pct	1.6582	2.03	3.366146	2.15	3.56513	1.76	2.918432	2.15	3.56513	2.55	4.22841	2.01	3.332982	1.2	1.98984	1.67	2.769194	1.59	2.636538
Na_ME-MS61_pct	1.348	2.02	2.72296	1.45	1.9546	2.44	3.28912	2.18	2.93864	0.09	0.12132	0.17	0.22916	0.53	0.71444	2.6	3.5048	1.78	2.3994
S_ME-MS61_pct	2.4972	0.01	0.024972	0.005	0.012486	0.08	0.199776	0.45	1.12374	1.58	3.945576	0.95	2.37234	1.61	4.020492	0.07	0.174804	0.16	0.399552
Ti_ME-MS61_pct	1.6681	0.651	1.085933	0.63	1.050903	0.684	1.14098	0.711	1.186019	0.295	0.49209	0.69	1.150989	0.606	1.010869	0.653	1.089269	0.696	1.160998
Total			36.96277		35.95118		34.00163		36.67356		36.17499		39.46617		35.62705		34.08702		33.03531
NOTE: The geochemical method of analysis (ICP_MS61) selected by Shanta does not involve the analysis of Silicon (Si) element																			
Ag_ME-MS61_ppm		0.02		0.02		0.04		0.12		0.3		0.15		0.35		0.05		0.05	
As_ME-MS61_ppm		3		5.5		6.5		11.1		21.1		31.2		137		4.5		23	
Ba_ME-MS61_ppm		90		180		320		70		190		270		200		50		100	
Be_ME-MS61_ppm		0.49		0.39		0.49		0.47		0.49		0.88		1.75		0.49		0.51	
Bi_ME-MS61_ppm		0.01		0.01		0.005		0.02		0.07		0.03		0.09		0.01		0.03	
Cd_ME-MS61_ppm		0.11		0.12		0.09		0.07		0.1		0.09		0.07		0.05		0.08	
Ce_ME-MS61_ppm		22.5		21		16.65		19.45		12.8		13.85		16.1		20.5		26.9	
Co_ME-MS61_ppm		35.8		34.1		27.7		26.9		24.1		25		27.7		30.3		30.3	
Cr_ME-MS61_ppm		27		26		24		18		25		20		21		22		22	
Cs_ME-MS61_ppm		0.51		2.47		1.36		2.17		2.08		4.65		7.9		0.18		1.12	
Cu_ME-MS61_ppm		55.9		41		55.3		81.4		120.5		55		55.1		43.1		117	
Ga_ME-MS61_ppm		20.1		18.9		18.1		15.85		11		20		17.85		20.1		20.3	
Ge_ME-MS61_ppm		0.07		0.09		0.11		0.08		0.06		0.09		0.09		0.09		0.09	
Hf_ME-MS61_ppm		2.1		1.8		2		2.4		1.4		2.6		2.3		2		2	
In_ME-MS61_ppm		0.067		0.063		0.059		0.05		0.039		0.058		0.053		0.055		0.066	
La_ME-MS61_ppm		9.9		8.8		6.3		8		5.3		5.4		6.5		8.9		11.5	
Li_ME-MS61_ppm		18.2		33.7		35.8		32.7		8.9		7.8		5.2		18		28	
Mn_ME-MS61_ppm		982		949		1070		896		1490		1230		1230		979		946	
Mo_ME-MS61_ppm		1.1		0.75		0.73		0.58		2.89		1		9.99		0.9		1.38	
Nb_ME-MS61_ppm		4.5		4		4.4		4.6		2.3		4.2		5.2		4.3		4.8	
Ni_ME-MS61_ppm		55		52.4		46.9		40.2		33.7		37.7		28.5		47		42.7	
P_ME-MS61_ppm		550		520		530		570		340		500		550		530		540	
Pb_ME-MS61_ppm		2.7		2.1		2.4		2.9		3.2		3.1		4.8		2.4		2.6	
Rb_ME-MS61_ppm		1.3		24.7		9.8		16		62.3		93.6		67.2		0.2		8.8	
Re_ME-MS61_ppm		0.003		0.003		0.006		0.005		0.003		0.005		0.005		0.007		0.008	
Sb_ME-MS61_ppm		0.13		1.06		0.26		1.12		0.96		1.38		1.72		0.09		0.54	
Sc_ME-MS61_ppm		24.9		23.6		21.9		21.4		14.5		20.9		19.7		22		23.2	
Se_ME-MS61_ppm		0.5		1		0.5		0.5		1		0.5		0.5		0.5		1	
Sn_ME-MS61_ppm		1.3		0.9		0.9		0.9		0.7		1		1		1		1.2	
Sr_ME-MS61_ppm		240		136.5		126.5		125.5		120		106		102		149		134.5	
Ta_ME-MS61_ppm		0.32		0.3		0.34		0.35		0.15		0.33		0.31		0.34		0.35	
Te_ME-MS61_ppm		0.025		0.025		0.025		0.025		0.16		0.025		0.12		0.025		0.025	
Th_ME-MS61_ppm		1.08		0.94		0.78		1.22		0.62		1.15		4.3		1.05		1.2	
Tl_ME-MS61_ppm		0.02		0.15		0.14		0.07		0.18		0.47		0.46		0.01		0.09	
U_ME-MS61_ppm		0.3		0.3		0.2		0.3		0.6		1.5		1.1		0.2		0.3	
V_ME-MS61_ppm		160		158		153		154		100		170		161		160		164	
W_ME-MS61_ppm		0.1		0.5		0.2		1.6		3.4		13.3		11.7		0.2		0.2	
Y_ME-MS61_ppm		21.6		15.9		14.5		15		9.8		14.3		15		21.7		23	
Zn_ME-MS61_ppm		109		114		95		84		45		61		28		90		100	
Zr_ME-MS61_ppm		81.2		65.3		63		92.4		50.1		90.2		79.4		65.4		64.6	
Au_ppm_d								0.02		0.05		0.04		0.23					
Au_ppmName_d								Au_AU-AA26_ppm		Au_AU-AA26_ppm		Au_AU-AA26_ppm		Au_AU-AA26_ppm					

	Std Oxide conversion factors	DDA35671	Oxide	DDA30564	Oxide	DDA30575	Oxide	DDA30578	Oxide	DDA35672	Oxide	DDA35673	Oxide	DDA35674	Oxide	DDA35675	Oxide	DDA35676	Oxide
Al_ME-MS61_pct	1.8895	6.92	13.07534	7.5	14.17125	5.67	10.71347	7.24	13.67998	6.28	11.86606	5.39	10.18441	6.54	12.35733	6.18	11.67711	6.61	12.4896
Ca_ME-MS61_pct	1.3992	5.11	7.149912	5.1	7.13592	7.69	10.75985	4.27	5.974584	6.4	8.95488	9.45	13.22244	13.45	18.81924	6.7	9.37464	6.37	8.912904
Fe_ME-MS61_pct	1	6.51	6.51	7.27	7.27	3.52	3.52	3.42	3.42	9.9	9.9	8.24	8.24	6.86	6.86	10.1	10.1	9.63	9.63
K_ME-MS61_pct	1.2046	0.17	0.204782	1.18	1.421428	2.26	2.722396	0.54	0.650484	0.03	0.036138	0.03	0.036138	0.01	0.012046	0.17	0.204782	0.55	0.662530
Mg_ME-MS61_pct	1.6582	1.87	3.100834	2.28	3.780696	0.93	1.542126	0.85	1.40947	3.46	5.737372	1.66	2.752612	1.19	1.973258	3.15	5.22333	3.44	5.704208
Na_ME-MS61_pct	1.348	1.96	2.64208	1.95	2.6286	0.19	0.25612	4.17	5.62116	1.46	1.96808	0.57	0.76836	0.03	0.04044	1.5	2.022	1.7	2.2916
S_ME-MS61_pct	2.4972	0.05	0.12486	0.28	0.699216	0.84	2.097648	0.07	0.174804	0.15	0.37458	0.07	0.174804	0.13	0.324636	0.14	0.349608	0.13	0.324636
Ti_ME-MS61_pct	1.6681	0.592	0.987515	0.691	1.152657	0.252	0.420361	0.309	0.515443	0.708	1.181015	0.605	1.009201	0.598	0.997524	0.742	1.23773	0.691	1.152657
Total			33.79532		38.25977		32.03196		31.44592		40.01812		36.38796		41.38447		40.1892		41.16813
NOTE: The geochemical method of analysis (ICP_MS61) selected by Shanta does not involve the analysis of Silicon (Si) element																			
Ag_ME-MS61_ppm		0.04		0.1		0.21		0.06		0.04		0.04		0.05		0.06		0.04	
As_ME-MS61_ppm		28.8		23		27.8		14.1		2		1.5		11.8		3.1		2.4	
Ba_ME-MS61_ppm		70		200		450		140		10		10		5		70		110	
Be_ME-MS61_ppm		0.53		0.4		0.65		0.51		0.32		0.51		0.62		0.45		0.39	
Bi_ME-MS61_ppm		0.02		0.01		0.03		0.02		0.005		0.005		0.005		0.005		0.005	
Cd_ME-MS61_ppm		0.09		0.07		0.1		0.11		0.18		0.23		0.17		0.1		0.12	
Ce_ME-MS61_ppm		17.5		15.3		29		20		12.45		11.95		13.9		20.6		17.7	
Co_ME-MS61_ppm		31.5		29.4		14.5		17.8		52.9		41.5		21.5		48.5		49.3	
Cr_ME-MS61_ppm		32		21		53		54		155		118		111		101		132	
Cs_ME-MS61_ppm		0.8		2.14		5.61		1.5		0.42		0.19		0.32		1.41		3	
Cu_ME-MS61_ppm		43.7		106		37.5		52.9		93.1		90.2		59.2		102.5		94.7	
Ga_ME-MS61_ppm		19.9		19.4		15.1		18.2		19.9		21.4		34.4		18.8		18.25	
Ge_ME-MS61_ppm		0.06		0.06		0.1		0.07		0.07		0.06		0.17		0.11		0.11	
Hf_ME-MS61_ppm		2		2.2		3		2		1.8		1.5		1.3		2.7		2.3	
In_ME-MS61_ppm		0.048		0.065		0.034		0.029		0.089		0.077		0.105		0.11		0.098	
La_ME-MS61_ppm		7.4		6		14.3		9		4.5		4.4		6.1		8.2		7.3	
Li_ME-MS61_ppm		24.6		24.9		15.2		10.2		15		6.6		14.8		11		17.2	
Mn_ME-MS61_ppm		902		1070		836		873		1500		1430		1520		1750		1560	
Mo_ME-MS61_ppm		0.96		0.76		0.64		0.61		0.62		1.16		0.39		0.64		0.41	
Nb_ME-MS61_ppm		4.1		5.2		3.2		3.2		3.8		3.7		3.5		4.5		4	
Ni_ME-MS61_ppm		53.9		43.8		54.2		44.7		121		92		68.3		72.1		79.6	
P_ME-MS61_ppm		460		700		380		350		400		400		390		530		490	
Pb_ME-MS61_ppm		3.4		3.6		4.7		2.6		2.4		1.7		1.8		2.3		2.8	
Rb_ME-MS61_ppm		2.2		13.6		90.3		14.7		0.4		0.4		0.4		5.2		24.7	
Re_ME-MS61_ppm		0.004		0.005		0.007		0.005		0.007		0.006		0.006		0.011		0.007	
Sb_ME-MS61_ppm		0.39		0.58		1.39		0.35		0.23		0.23		0.5		0.4		0.12	
Sc_ME-MS61_ppm		21.6		20.6		9.6		12.9		39.3		31.9		25.5		44.7		45.4	
Se_ME-MS61_ppm		0.5		1		1		1		1		0.5		0.5		1		1	
Sn_ME-MS61_ppm		0.8		1.4		1.3		1.1		0.8		1		1.3		1.1		1.2	
Sr_ME-MS61_ppm		201		62.8		92.1		113		142.5		213		43.3		110.5		179.5	
Ta_ME-MS61_ppm		0.32		0.4		0.31		0.28		0.24		0.23		0.24		0.32		0.26	
Te_ME-MS61_ppm		0.025		0.07		0.025		0.025		0.025		0.025		0.025		0.025		0.025	
Th_ME-MS61_ppm		0.92		0.9		2.02		1.43		0.33		0.3		0.26		1.86		1.55	
Tl_ME-MS61_ppm		0.03		0.18		0.4		0.11		0.02		0.01		0.02		0.05		0.13	
U_ME-MS61_ppm		0.2		0.3		0.5		0.3		0.1		0.1		0.1		0.5		0.4	
V_ME-MS61_ppm		142		203		59		89		296		246		253		312		290	
W_ME-MS61_ppm		0.1		0.9		4.2		0.3		0.1		0.1		1.6		0.2		0.3	
Y_ME-MS61_ppm		19.4		11.3		13.2		10.8		29.4		25.5		22.5		32.3		29.9	
Zn_ME-MS61_ppm		84		144		62		67		108		81		80		109		119	

	Std Oxide conversion factors	DDA30588	Oxide	DDA30596	Oxide	DDA30602	Oxide	DDA30605	Oxide	DDA35678	Oxide	DDA35679	Oxide	DDA30619	Oxide
Al_ME-MS61_pct	1.8895	6.33	11.96054	7.63	14.41689	7.14	13.49103	6.17	11.65822	6.92	13.07534	6.64	12.54628	5.12	9.67424
Ca_ME-MS61_pct	1.3992	7.03	9.836376	6.24	8.731008	4.66	6.520272	8.43	11.79526	5.51	7.709592	5.39	7.541688	10.45	14.62164
Fe_ME-MS61_pct	1	8.51	8.51	11.5	11.5	6.56	6.56	8.3	8.3	5.74	5.74	7.96	7.96	8.13	8.13
K_ME-MS61_pct	1.2046	0.08	0.096368	1.16	1.397336	0.13	0.156598	0.26	0.313196	0.07	0.084322	0.06	0.072276	0.91	1.096186
Mg_ME-MS61_pct	1.6582	2.04	3.382728	1.86	3.084252	2.43	4.029426	1.82	3.017924	2.43	4.029426	1.82	3.017924	1.77	2.935014
Na_ME-MS61_pct	1.348	1.39	1.87372	0.77	1.03796	2.55	3.4374	1.22	1.64456	1.95	2.6286	2.29	3.08692	0.07	0.09436
S_ME-MS61_pct	2.4972	0.1	0.24972	6.69	16.70627	0.1	0.24972	0.41	1.023852	0.05	0.12486	0.12	0.299664	1.4	3.49608
Ti_ME-MS61_pct	1.6681	0.678	1.130972	0.903	1.506294	0.598	0.997524	0.633	1.055907	0.453	0.755649	0.681	1.135976	0.52	0.867412
Total			37.04042		58.38		35.44197		38.80891		34.14779		35.66073		40.91493
NOTE: The geochemical method of analysis (ICP_MS61) selected by Shanta does not involve the analysis of Silicon (Si) element															
Ag_ME-MS61_ppm		0.01		0.42		0.01		0.05		0.005		0.02		0.3	
As_ME-MS61_ppm		13.6		165		17.9		40.5		1.6		26.8		69.1	
Ba_ME-MS61_ppm		30		200		70		50		40		20		200	
Be_ME-MS61_ppm		0.28		0.7		0.67		0.32		0.44		0.27		0.3	
Bi_ME-MS61_ppm		0.01		0.01		0.02		0.32		0.01		0.005		0.005	
Cd_ME-MS61_ppm		0.15		0.08		0.03		0.32		0.07		0.1		0.15	
Ce_ME-MS61_ppm		13.55		7.91		46.2		0.32		22.1		12.6		13.3	
Co_ME-MS61_ppm		45.5		54.1		36		0.32		30.7		45.1		39	
Cr_ME-MS61_ppm		123		167		49		0.32		55		123		90	
Cs_ME-MS61_ppm		1.21		5.98		2.06		0.32		1.31		0.57		6.2	
Cu_ME-MS61_ppm		83.1		102.5		45.5		0.32		40.6		81.7		73.8	
Ga_ME-MS61_ppm		17.4		18.9		19.05		0.32		18.6		17.05		14.85	
Ge_ME-MS61_ppm		0.08		0.06		0.11		0.32		0.08		0.08		0.08	
Hf_ME-MS61_ppm		1.2		1.2		3.2		0.32		1.6		1.7		1.1	
In_ME-MS61_ppm		0.088		0.081		0.063		0.32		0.038		0.075		0.061	
La_ME-MS61_ppm		5		2.6		21.2		0.32		9.5		4.6		5.1	
Li_ME-MS61_ppm		30.8		45.7		26.5		0.32		23.2		35.9		31.3	
Mn_ME-MS61_ppm		1450		1360		1010		0.32		919		1330		1750	
Mo_ME-MS61_ppm		0.29		0.92		0.7		0.32		0.84		0.21		0.24	
Nb_ME-MS61_ppm		3.9		4		8.2		0.32		3.9		3.7		2.9	
Ni_ME-MS61_ppm		97.1		127.5		79.1		0.32		70.3		100		76.4	
P_ME-MS61_ppm		420		580		890		0.32		670		440		350	
Pb_ME-MS61_ppm		2		6.1		2.2		0.32		2.4		1.8		8.8	
Rb_ME-MS61_ppm		3.3		12.4		3.8		0.32		1		3.2		47	
Re_ME-MS61_ppm		0.005		0.009		0.007		0.32		0.005		0.007		0.008	
Sb_ME-MS61_ppm		0.78		4.82		0.73		0.32		0.48		0.38		1.26	
Sc_ME-MS61_ppm		40.8		39.2		25.8		0.32		21.1		38.8		29.9	
Se_ME-MS61_ppm		1		1		0.5		0.32		1		1		1	
Sn_ME-MS61_ppm		0.9		1		1.3		0.32		0.7		0.9		0.7	
Sr_ME-MS61_ppm		98.1		119		125		0.32		222		57.7		76.4	
Ta_ME-MS61_ppm		0.25		0.26		0.58		0.32		0.27		0.25		0.2	
Te_ME-MS61_ppm		0.025		0.025		0.025		0.32		0.025		0.025		0.58	
Th_ME-MS61_ppm		0.36		0.24		3.91		0.32		0.82		0.34		0.22	
Tl_ME-MS61_ppm		0.04		0.58		0.06		0.32		0.03		0.02		0.22	
U_ME-MS61_ppm		0.1		0.1		0.9		0.32		0.2		0.1		0.05	
V_ME-MS61_ppm		264		354		159		0.32		144		259		200	
W_ME-MS61_ppm		0.3		2.2		0.3		0.32		0.1		0.1		1.9	
Y_ME-MS61_ppm		28.8		10.1		25.5		0.32		12.3		15.1		14.7	
Zn_ME-MS61_ppm		112		94		87		0.32		76		104		93	
Zr_ME-MS61_ppm		33.3		41.9		124		0.32		65.2		56.2		34.1	
Au_ppm_d		0.005		0.04		0.01		0.32						0.03	
Au_ppmName_d		Au_AU-AA26_ppm		Au_AU-AA26_ppm		Au_AU-AA26_ppm		0.32						Au_AU-AA26_ppm	

Appendix B: Summary of Rock Names and Mineralogy from Mason lab. Report

Summary of rock names and mineralogy from Mason lab. Report (Mason, 2018)

SAMPLE	ROCK NAME	MINERALOGY*
Primary**	Metamorphic/	Vein lets / fracture
Alteration***	seals***	
RAMBI PROSPECT		
DDA30529; Carbonate-hematite altered	Cpx, bio-Car(cal), qtz,	
LZD0001, 95.9m; lamprophyre iul	opq(mt,hem)	
DDA30530; Fractured and altered me-ta-layered	Qtz Flm(alb), ser, car, py,	Qtz, car(cal), py;
LZD0001, 126.2m; felsic ?tuff	leu	Car(cal), py, cpy,
vflt		sph
DDA30551; Carbonate-chlorite-quartz altered	Car(cal), qtz, chl, leu,	
LZD0001, 215.5m; lamprophyre iul	opq(?mt,hem)	
DDA30551; Albite-carbonate-hematite altered	Qtz	Alb, car(cal), qtz, ser,
LZD0001, 215.5m; granitoid	hem, chl,	
ifg	opq(?mt,hem)	

DDA30552; Albite-clinozoisite-chlorite altered	Qtz, apa	Alb, clz, chl, leu,
LZD0001, 256.7m; meta-porphyritic ?diorite iid	opq(?sulf)	
DDA30553; Carbonate-chlorite altered	Crsp	Car (?Fecar), chl,
LZD0001, 317.9m; lamprophyre	car(cal), tic,	
iul	opq(?mt,hem), leu	
iul	opq(?mt,hem), leu	
DDA30554; Carbonate-talc-hematite altered	Bio, cpx, Kf, Car, car(cal), tic,	Car(cal), Kf
LZD0001, 318.6m; lamprophyre iid	opq(mt)	opq(hem)
DDA30555; LZD0001, 398.2m; imd	Fractured and veined, altered ?meta¬micro-dolerite:	
High-intensity carbonate-sericite-	Qtz, apa	Car(?dol), ser, flm(qtz), -
sulfide altered ?meta-micro- dolerite	leu(rut) py	
Early quartz-carbonate veins		Qtz, car(dol)
Late carbonate-chlorite-sulfide veinlets and fracture seals		Car(dol), chl, py, qtz

NOTES

*: Minerals are listed in each paragenesis according to approximate decreasing abundance.

**: Only primary minerals currently present in the rock are listed. Others may have been present, but are altered. ': Earlier parageneses are separated from later parageneses by a semicolon.

Mineral abbreviations

Act = actinolite; alb = albite; apa = apatite; bio = biotite; cal = calcite; car = carbonate minerals; chl = chlorite; clz = clinozoisite; cpx = clinopyroxene; cpy = chalcopyrite; dol = dolomitic carbonate mineral; Fe-car = Fe-carbonate mineral; flm = fine-grained felsic mosaic (mostly albite); hem = hematite; ilm = ilmenite; Kf = K-feldspar; leu = leucoxene (fine-grained Ti minerals); mt = magnetite; opq = opaque minerals; pla = plagioclase; po = pyrrhotite; preh = prehnite; py = pyrite; qtz = quartz; rut = rutile; ser = sericite; sph = sphalerite; sulf = sulfide minerals; tic = talc; tou = tourmaline; zoi = zoisite; ?min = uncertain mineral identification; min? = uncertain mineral paragenesis.